Role of competition between slip and twinning in nanoscale deformation of sapphire

N. Tymiak,[1,*] D. Chrobak,[1,†] W. Gerberich,[2] O. Warren,[3] and R. Nowak[1,‡]
[1]*Nordic Hysitron Laboratory, Helsinki University of Technology, 02015 HUT, Helsinki, Finland*
[2]*CEMS, University of Minnesota, Minneapolis, Minnesota 55455, USA*
[3]*Hysitron, Inc., Minneapolis, Minnesota 55344, USA*
(Received 6 January 2009; revised manuscript received 26 February 2009; published 26 May 2009)

Insights into the initiation of plasticity under contact loading of *A* and *M* planes of sapphire are provided by finite element analysis of the resolved shear stress acting on basal slip and basal twinning systems and by the evaluation of acoustic emission signals associated with the onset of plasticity. The analysis of acoustic emission activity utilizes wavelet-based signal representation in the joint time-frequency domain. The proposed model invoking loading-rate-dependent competition between basal slip and basal twinning predicts different yield-point mechanisms for *A* and *M* planes. The predicted mechanisms are consistent with the experimental plasticity initiation patterns. Room-temperature values of critical shear stress of 12.9–13.9 GPa for basal slip and 12.6–14.4 GPa for basal twinning derived from application of finite element analysis to the results of nanoindentation experiments are compared with the values expected from the results of theoretical modeling and extrapolation of high-temperature experimental results.

DOI: 10.1103/PhysRevB.79.174116 PACS number(s): 46.80.+j, 62.25.−g, 43.60.+d, 62.20.F−

I. INTRODUCTION

The use of sapphire in advanced technologies[1,2] stimulates interest in the mechanical response of Al_2O_3. Whether an ultimate goal is preserving component integrity or a deliberate defect generation, understanding the mechanisms of plasticity initiation is crucial. Recognized for its ability to provide valuable information about plasticity onset mechanisms,[3–6] nanoindentation becomes even more powerful when combined with the acoustic emission (AE) monitoring. AE enables insight into kinetics and time span of physical events often not discernable from nanoindentation load-depth response. Highly localized AE sensing[7,8] utilizing AE sensor integrated into an indenter tip enables monitoring of nanoscale contacts.[9–11]

With the utilization of continuum and atomistic approaches, nanoindentation offers solutions for applications invoking novel materials and/or materials in ultrasmall volumes. Considerable attention continues to be devoted to the yield point, a transition from the apparently elastic to elastic-plastic regime. The yield-point transition is evident from a characteristic indentation curve discontinuity. For isotropic materials, analytical[4,5] and numerical[12] analyses demonstrated that at the yield-point resolved shear stress (RSS) acting on slip systems approaches theoretical strength of the evaluated materials. Given elastic anisotropy of sapphire, analytical solutions derived with the assumption of elastic isotropic behavior are not sufficient for the evaluation of RSS at the onset of plasticity. To date, the first and only finite element analysis (FEA) accounting for the elastic anisotropy of sapphire[13] focused on the evaluation of rhombohedral twinning previously discussed as one of the possible participants of the yield-point mechanism in sapphire.

The present study applies FEA of indentation-induced stress combined with the evaluation of AE activity to the evaluation of the yield-point phenomenon in sapphire. Previous studies associate the yield point in Al_2O_3 with either nucleation of first dislocations,[3] twinning,[14] or activation of basal kink bands.[15] Concerning the basal kinking model,[15] evaluations of room-temperature contacts provided evidence of twinning and basal and nonbasal slip systems as reviewed by Tymiak and Gerberich,[16] but never discerned the presence of basal kink bands. Given difficulties in resolving features of nanoindentation-induced plasticity, inability to provide experimental evidence of basal kink bands generated by room-temperature contact loading of Al_2O_3 weakens standing of the basal kinking model[15] but cannot be used as an argument refuting its validity entirely. Page *et al.*[3] and Nowak *et al.*[14] presented convincing experimental findings supporting models proposed in their studies.[3,14] However, like the basal kinking model,[15] those models[3,14] would not rationalize findings of the studies utilizing the highly localized AE monitoring.[8,9]

Common for the models,[3,14,15] the yield-point mechanism was presumed to be the same for all surface orientations of sapphire. In contrast, pattern of AE activity was different for each of the four surfaces $C(0001)$, $R(1\bar{1}02)$, $A(1\bar{2}10)$, and $M(10\bar{1}0)$,[8,9] indicating different plasticity initiation mechanisms. Examination of experimental results combined with the elastic isotropic analysis[16,17] allowed narrowing of the possible yield-point mechanisms for *A* and *M* planes to a competition between basal slip $[(0001), 1/3\langle 11\bar{2}0\rangle]$ and basal twinning [twinning plane $K_1=(0001)$, twinning direction $\eta_1=\langle 10\bar{1}0\rangle$].

For *C* and *R* planes, there was no distinct effect of loading rate on P_{yield} and, consistent with the absence of $\tau_{\text{basal tw}}$ localization for those planes, surface traces of basal twins were not discernable.[16] Supporting the involvement of basal twinning in the yield point for the *M* plane, linear surface features activated at the yield point were identified as basal twins.[18] Additional "post-yield-point" sets of basal twins were activated at loads significantly exceeding P_{yield}, the yield-point load.[9,18] Locations of basal twins were consistent with the predicted positions of the highest localization of $\tau_{\text{basal tw}}$, RSS for basal twinning.[16] In agreement with the loading-rate effect on twinning previously observed for other

materials,[19] increasing loading rate[9,18] resulted in P_{yield} decreasing for the *M* plane. For the *A* plane, P_{yield} was independent of loading rate[9] and basal twins appeared to be activated only after the yield point. The above *ex situ* information gleaned from indentation curves and micrographs of indentation impressions indicated that basal twinning plays an important role in the earliest stages of plasticity for *A* and *M* planes and prompted a hypothesis that the yield-point mechanisms are different for those planes.[9]

Further support of this hypothesis was obtained from scrutiny of AE waveforms in the time domain providing *in situ* information about the processes involved in the onset of plastic deformation. The characteristic chosen to discriminate between different types of AE signals was the emission shape factor (ESF), a parameter describing the distribution of signal energy over the signal time span. Highly transient rapidly decaying signals yield the highest ESF values. Two types of AE signals observed for *A* and *M* planes included sharply decaying transients[9] referred to as "type 1 pattern" (ESF=7.2–9.4) and "type 2 pattern" signals indicative of process involving a period of sustained energy release (ESF=3.1–6.9). Signal attenuation time for the type 2 pattern signals was on average twice longer than signal attenuation time for the type 1 pattern signals. Type 2 pattern was similar to AE signals associated with twinning involving considerable twin growth.[20] In line with the studies by Bovenko *et al.*[21] and Richeton *et al.*[22] noting similar distinctions between AE signatures of slip and twinning in hcp metals, Tymiak *et al.*[9] ascribed type 1 and type 2 pattern signals to slip and twinning, respectively. For *C* and *R* planes, type 2 pattern signals were never detected, in agreement with the absence of discernible traces of basal twins for those planes.[8,9]

For both *A* and *M* planes, sequences of type 1 pattern and type 2 pattern signals were detected at the onset of contact-induced plasticity. However, the sequences and their dependence on loading rate were distinctively different for *A* and *M* surfaces, indicating differences in plasticity initiation mechanisms. At loading rate of 0.1 mN/s, the AE signal associated with the yield point for *A* and *M* planes was always a single type 1 pattern as shown in Fig. 1(a). As the loading rate increased from 0.25 to 1.6 mN/s, AE activity for the *A* plane remained unchanged, while for the *M* plane, a "two-step signal" rather than a single type 1 pattern was increasingly often detected at the yield point (in 15%, 20%, 80%, and 90% of tests for loading rates of 0.25, 0.5, 1.0, and 1.6 mN/s, respectively). The two-step signal included a type 2 pattern immediately followed by a type 1 pattern as shown in Fig. 1(b). With the load increased to 200–400 % P_{yield}, type 2 pattern signals were observed for both *A* and *M* planes.

The above experimental results suggest that with increasing loading rates, the yield-point mechanism for the *M* plane changes from basal slip dominated to basal twinning dominated. Such mechanism change is consistent with the models[19,23] defining basal slip and basal twinning in Al_2O_3 as competitive processes with the common initial stage. Depending on the strain rate, $\dot{\varepsilon}$ and on the levels of $\tau_{basal\ sl}$ (RSS for basal slip) and $\tau_{basal\ tw}$, the initial stage evolves to either basal slip or basal twinning.[19] The common stage involves forming a leading $\frac{1}{3}\langle 10\bar{1}0\rangle$ and $\frac{1}{3}\langle 01\bar{1}0\rangle$ trailing partial dislocations. If the trailing partial becomes locked, the leading partial may create a basal twin.[19] Alternatively, the trailing partial can climb up to recombine with the leading partial and form a perfect basal plane partial dislocation.[19] Climb of a trailing partial is facilitated by diffusion, a time-dependent process affected by stress and temperature.[19] As climb of a trailing partial leading to basal slip is favored by decreasing strain rate, increasing $\dot{\varepsilon}$ facilitates twinning. Distribution of preexisting flaws is also a factor affecting the competition between slip and twinning. Experimental observations suggest that twinning is strongly influenced by the presence of surface flaws facilitating heterogeneous twin activation.[24]

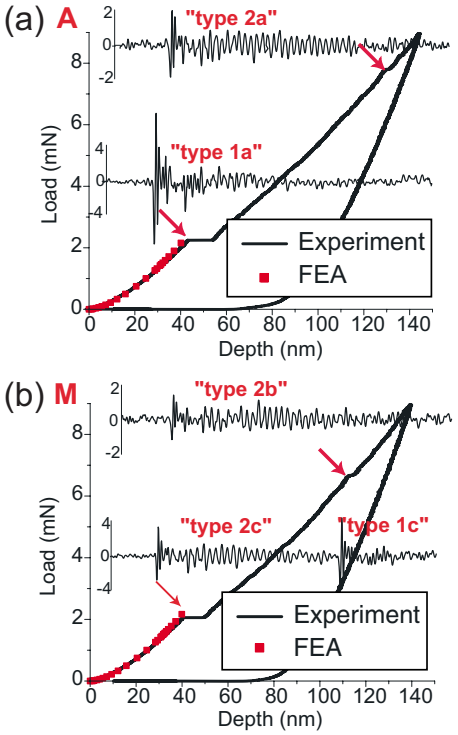

FIG. 1. (Color online) Load-displacement curves with the respective patterns of AE activity for (a) *A* plane and (b) *M* plane of sapphire. AE waveforms correspond to indentation curve discontinuities denoted by arrows. Each AE waveform is shown over a 2 ms time span and has units of mV. The measured mV output gives relative information about the actual AE waveform. Calibration of the AE-sensing system would allow obtaining of the corresponding surface displacement detected by the AE sensor. Dotted lines indicate FEA-simulated load-depth response. Categories of AE signal types 1a, 1b, and 1c and types 2a, 2b, and 2c are defined in Table I.

In order to minimize possible effects of surface flaws in the studies by Tymiak *et al.*,[8,9] *A* and *M* planes with surface roughness of less than 1 nm were used and sets of experiments were performed at multiple locations for both *A* and *M* surfaces. Given identical experimental conditions for *A* and *M* planes (topography of pristine surfaces, temperature, indenter tips, and loading rates), a conclusion can be drawn that the observed differences between plasticity initiation patterns for *A* and *M* planes[8,9] were determined mainly by the peculiarities of RSS distributions acting on slip and twinning systems. Such conclusion was supported by the results

of isotropic elastic analysis predicting conditions for activation of basal twinning to be more favorable for the *M* plane.[16,17]

However, the authors[16,17] acknowledged the possibility of errors stemming from ignoring elastic anisotropy of sapphire. Given similar $\tau^{max}_{basal\ tw}$ and $\tau^{max}_{basal\ sl}$ (maximum values of $\tau_{basal\ tw}$ and $\tau_{basal\ sl}$) predicted for *A* and *M* planes by the isotropic elastic analysis, Tymiak and Gerberich[16,17] recommended FEA evaluation for clarifying why basal twinning at the yield point is favored only for the *M* plane, while for both *A* and *M* planes basal twins can be activated at loads of 200–400 % P_{yield}. Another drawback noted by Tymiak and Gerberich[16,17] was that RSS distributions were not determined at the surface ($z=0$) where the analytical solution does not exist. However, examination of $\tau_{basal\ tw}$ at the surface is crucial since twinning is known to be activated mainly at the surface.[24] In order to remove uncertainties associated with not accounting for the elastic anisotropy of sapphire and inability to assess values of RSS at the surface, the present study performed FEA evaluation of indentation-induced stress.

As the analysis of AE activity is concerned, the distinction between different types of waveforms associated with the plasticity initiation in sapphire was previously examined in terms of time-domain waveform characteristics.[9] The present study evaluates the patterns of AE activity in joint time-frequency domain (JTFD). JTFD representation demonstrating change in frequency content over the signal time span is used for the analysis of nonstationary signals.[7,25,26]

II. PROCEDURES

A. Finite element analysis

FEA was performed with the commercial ABAQUS FEA software. RSS definitions followed procedures of the study by Tymiak and Gerberich.[16] The calculations used elastic constants for Al_2O_3 recently verified by Winey and Gupta,[27] elastic constants for diamond as reported by Oliver and Pharr,[28] and a diamond-sapphire friction coefficient of 0.085.[29] To assure accuracy of input for FEA calculations, shape of the indenter tip utilized in the AE-monitored nanoindentation experiments[9] (90° cone of approximate 500 nm end radius) was assessed by imaging with the silicon calibration grating TGT01 and subsequent curve fitting of the obtained indenter tip profile at distances from 2 to 50 nm (with 40 nm corresponding to average indentation depth at the yield point) from indenter apex. Based on the evaluations indicating the tip radius changing from 270 to 520 nm over the examined depth range, indenter tip geometry was modeled as a sphere of 370 nm radius. Mesh size refinement and sample and indenter dimensions were increased up to the values past which there were no discernable effects of mesh refinement and increase in sample and indenter dimensions on the resulting solution. Given mean P_{yield} values of 2.2 and 1.8 mN for *A* and *M* planes, respectively,[9] calculations were carried up to 2.1 mN indentation load, yielding a mean indentation pressure of 44 GPa. Validity of the FEA model was verified for a limiting case of spherical indentation into isotropic medium with the resulting deviation of the calculated stress field from analytical solution[30] less than 3%. A comparison between experimental and FEA-simulated load-displacement curves is shown in Fig. 1. FEA-derived $\tau_{basal\ tw}$ distributions were compared with the experimental patterns of surface traces of basal twins as shown in Fig. 2 and as reported previously.[14,18]

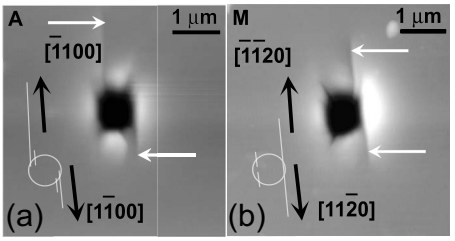

FIG. 2. Scanning probe microscopy (SPM) images of the distributions of surface traces of basal twins for (a) *A* and (b) *M* surface orientations. White arrows point toward surface traces of basal twins. Drawings in left lower corners represent schematics of distributions of surface traces of basal twins (white straight lines) with respect to the edges of indentation impressions (white circles).

B. Analysis of AE activity

The analysis was performed on AE signals detected with the commercial AE-monitoring system[7,8] (TriboAE™, Hysitron, Inc.) utilizing a conical AE-sensing indenter tip with the tip shape discussed in Sec. II A. Nanoindentation experiments up to 9 mN peak loads were performed at loading rate of 1 mN/s. AE sensing was carried out at 100–1200 kHz bandwidth and 10 MHz sampling frequency as detailed by Tymiak *et al.*[8] AE activity analysis was restricted to signals detected in experiments with $P_{yield}=2\pm0.2$ mN, comparable with the mean values for *A* and *M* planes.[9] The evaluated type 1 and type 2 pattern signals were divided into six categories (type 1a, type 1b, type 1c, type 2a, type 2b, and type 2c) specified in Table I and denoted in Fig. 1. The categories were defined by surface orientation (*A* or *M*), instance of signal detection (during or after the yield point), and pattern type (single type 1, single type 2, type 1 in a two-step signal, or type 2 in a two-step signal).

The selected AE signals were represented in JTFD using AGU-VALLEN software.[31] JTFD representation is a map indicating how distribution of signal energy between different frequencies changes over the signal time span. The details of the underlying wavelet-based signal decomposition are addressed by Suzuki *et al.*[32] The present study used frequency resolution of 10 kHz and wavelet size of 200 samples.

III. RESULTS AND DISCUSSION

A. Finite element analysis

1. Conditions required for the activation of basal twins

The present authors assume that activation of a basal twin at a given spatial position is possible if $\tau_{basal\ tw}$ exhibits a sufficient degree of localization and $\tau^{Cr}_{basal\ tw}(\dot{\varepsilon})$ can be attained before reaching $\tau^{Cr}_{basal\ sl}(\dot{\varepsilon})$ at this position. The latter requirement implies $\tau_{basal\ tw}/\tau_{basal\ sl} > \tau^{Cr}_{basal\ tw}(\dot{\varepsilon})/\tau^{Cr}_{basal\ sl}(\dot{\varepsilon})$.

TABLE I. Subcategories of type 1 and type 2 pattern AE signals. "After yield point" refers to signal detection at loads significantly exceeding the yield-point load (200–400 % of P_{yield}) as shown in Fig. 1. "Two-step signal" denotes a sequence of type 2c pattern immediately followed by type 1c pattern such as seen in Fig. 1(b).

Signal	Plane	Detected	Pattern in time domain	Shown in
Type 1a	*A*	Yield point	Single type 1	Figs. 1(a) and 4(a)
Type 1b	*M*	Yield point	Single type 1	Fig. 4(b)
Type 1c	*M*	Yield point	Type 1 in two-step signal	Figs. 1(b) and 4(c)
Type 2a	*A*	After yield point	Single type 2	Figs. 1(a) and 4(d)
Type 2b	*M*	After yield point	Single type 2	Fig. 4(e)
Type 2c	*M*	Yield point	Type 2 in two-step signal	Figs. 1(b) and 4(f)

2. Positions evaluated for the possibility of basal twin activation

According to the results of FEA calculations, $\tau^{max}_{basal\ tw}$ for *A* and *M* planes is attained at depths $z=85$ nm below the surface where localization of $\tau_{basal\ tw}$ occurs under the edge of contact as shown in Figs. 3(a) and 3(b). Additional positions of $\tau_{basal\ tw}$ localization are at $z=0$ as evident from Figs. 3(c) and 3(d).

3. Comparison between FEA predictions and experimental patterns of twin traces

As seen from Fig. 2(a), basal twins for the *A* surface initiate at the edge of contact and extend along $[1\bar{1}00]$ and $[\bar{1}100]$ directions, forming a pattern antisymmetric with respect to the (0001) axis. Origin of the observed antisymmetry is apparent from the evaluation of $\tau_{basal\ tw}$ and $\tau_{basal\ tw}/\tau_{basal\ sl}$ at $z=85$ nm presented in Figs. 3(a) and 3(e). At the position $\mathbf{a}_1$ where $\tau^{max}_{basal\ tw}$ is reached, $\tau_{basal\ tw}/\tau_{basal\ sl}=0.9$. A conclusion can be drawn that $\tau_{basal\ sl}$ can be reached at this position before attaining $\tau_{basal\ tw}$ and, therefore, activation of basal twins is not favored when $\tau^{Cr}_{basal\ tw}(\dot{\varepsilon})/\tau^{Cr}_{basal\ sl}(\dot{\varepsilon})=0.9$. Twin activation and extension is more likely at the locations denoted as $\mathbf{a}_2$ where $\tau_{basal\ tw}/\tau_{basal\ sl}=1.1$. The $\mathbf{a}_2$ positions form antisymmetric pattern consistent with the arrangement presented in Fig. 2(a). The distributions $\tau_{basal\ tw}$ and $\tau_{basal\ tw}/\tau_{basal\ sl}$ at $z=0$ shown in Figs. 3(c) and 3(g) also are consistent with the experimentally observed antisymmetry. On the right side of indentation impression, conditions for twin extension are more favorable along $[1\bar{1}00]$ direction where $\tau_{basal\ tw}$ decays more slowly and the $\tau_{basal\ tw}/\tau_{basal\ sl}$ is considerably higher than $\tau_{basal\ tw}/\tau_{basal\ sl}$ along the $[\bar{1}100]$ direction as evident

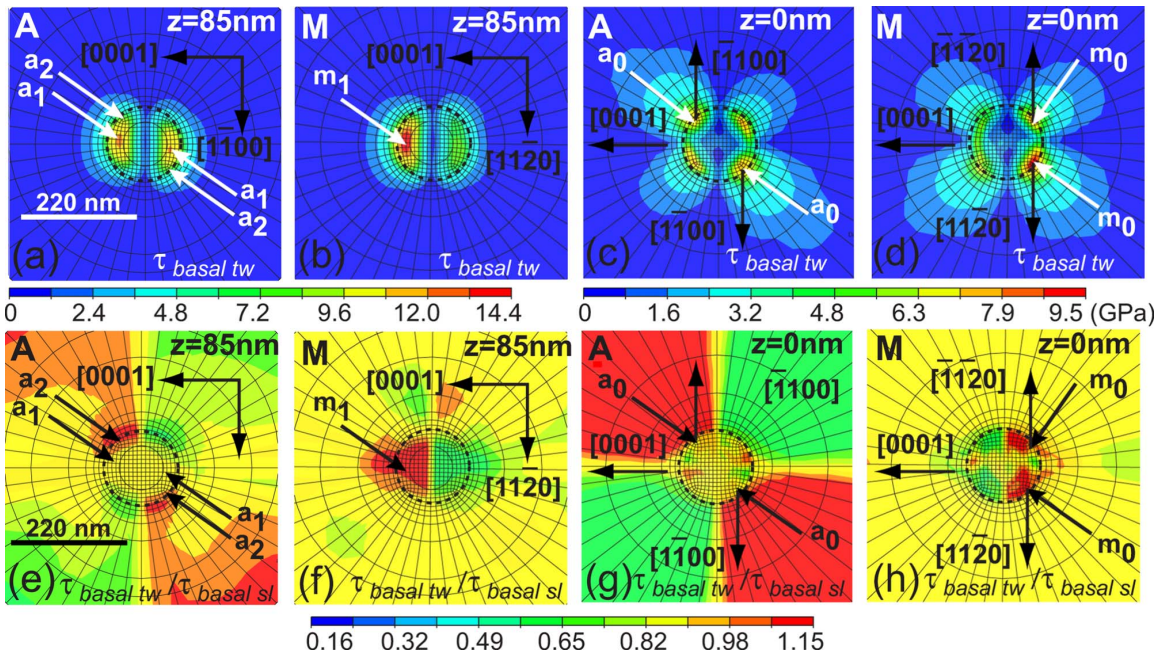

FIG. 3. (Color online) FEA evaluation of the possibility of basal twin activation for *A* and *M* surface orientations. The analysis simulates indentation experiments (Ref. 9) utilizing a 90° conical indenter tip of approximately 500 nm end radius and indentation load of 2.1 mN. Dotted circles denote projected edges of indentation contact areas. Distributions of $\tau_{basal\ tw}$, RSS acting on basal twinning systems, are shown in (a)–(d). Distributions of the ratio $\tau_{basal\ tw}/\tau_{basal\ sl}$ are shown in (e)–(h). Values of $\tau_{basal\ tw}$ and $\tau_{basal\ tw}/\tau_{basal\ sl}$ are determined at the surface ($z=0$ nm) and at depth $z=85$ nm below the surface where maximum of $\tau_{basal\ tw}$ is attained.

from Figs. 3(c) and 3(g). The opposite is true on the left side of indentation impression where twin extension along the $[\bar{1}100]$ direction is favored.

For the M plane, decay of $\tau_{\text{basal tw}}$ is the same along $[\bar{1}\bar{1}20]$ and $[11\bar{2}0]$ directions and the distribution $\tau_{\text{basal tw}}/\tau_{\text{basal sl}}$ is symmetric with respect to the (0001) axis, as seen from Figs. 3(b), 3(d), 3(f), and 3(h). Consequently, the pattern of basal twins is expected to be symmetric with respect to (0001) axis, in agreement with Fig. 2(b) and with the previous experimental findings.[14,18]

The above analysis indicates that the differences in surface topography patterns observed for A and M surfaces (shown in Fig. 2 and reported in previous studies[8,9,14,18]) are justified by the features of $\tau_{\text{basal tw}}$ and $\tau_{\text{basal tw}}/\tau_{\text{basal sl}}$ distributions. Particularly, 18% difference in $\tau_{\text{basal tw}}/\tau_{\text{basal sl}}$ ratio (0.9 at the positions $\mathbf{a}_1$ as compared to 1.1 at the positions $\mathbf{a}_2$ and $\mathbf{a}_0$) determines the preference for antisymmetry of basal twin extension following $[1\bar{1}00]$ and $[\bar{1}100]$ directions along the opposite sides of indentation impressions for the A plane. Consistency of the surface topography patterns for A and M surfaces reported by Nowak *et al.*[14,18] and in the subsequent evaluations[8,9] utilizing samples from different sources and different indenter tip radii [$R=5$ μm,[14,18] $R=0.5$ μm (Refs. 8 and 9)] suggests that those patterns[8,9,14,18] are not merely a consequence of surface flaws.

4. Yield-point mechanisms

Further analysis of the FEA-derived $\tau_{\text{basal tw}}$ and $\tau_{\text{basal tw}}/\tau_{\text{basal sl}}$ distributions suggests that conditions for activating basal twinning at the yield point are more favorable for the M plane than for the A plane. For $P_{\text{yield}}=2.1$ mN, $\tau^{\max}_{\text{basal tw}}=14.4$ GPa and $\tau_{\text{basal tw}}/\tau_{\text{basal sl}}=1.1$ at the position $\mathbf{m}_1$ where $\tau^{\max}_{\text{basal tw}}$ is attained. For the A plane, $\tau^{\max}_{\text{basal tw}}=12.6$ GPa (1.8 GPa or 12% lower than for the M plane) and $\tau_{\text{basal tw}}/\tau_{\text{basal sl}}=0.9$ (18% lower than for the M plane) at the position $\mathbf{a}_1$ where $\tau^{\max}_{\text{basal tw}}$ is attained. At $z=0$, the highest $\tau_{\text{basal tw}}$ for the M plane is 9.5 GPa at the position $\mathbf{m}_0$ in Fig. 3(d) as compared to 8 GPa for the A plane at the position $\mathbf{a}_0$ in Fig. 3(c).

Results of Sec. III A 3 indicate that the differences in $\tau_{\text{basal tw}}$ and 18% difference in $\tau_{\text{basal tw}}/\tau_{\text{basal sl}}$ values are sufficient to generate distinguishable and consistent surface topography patterns for A and M planes. Therefore, it is reasonable to conclude that the differences in $\tau_{\text{basal tw}}$ and $\tau_{\text{basal tw}}/\tau_{\text{basal sl}}$ distributions are sufficient to produce discernable and reproducible effects on the yield-point mechanisms. Based on such assumption, the present authors propose the following model justifying the experimentally observed differences in plasticity initiation patterns for A and M planes.

It is hypothesized that at the lowest loading rate invoked in the study by Tymiak *et al.*,[9] $\tau^{\text{Cr}}_{\text{basal tw}}(\dot{\varepsilon})/\tau^{\text{Cr}}_{\text{basal sl}}(\dot{\varepsilon})>1.1$. Under such conditions, basal twinning cannot be activated prior to activation of basal slip and, consequently, basal slip determines the yield point for A and M planes giving rise to type 1a and type 1b signals. Increasing loading rates decrease $\tau^{\text{Cr}}_{\text{basal tw}}(\dot{\varepsilon})/\tau^{\text{Cr}}_{\text{basal sl}}(\dot{\varepsilon})$ below 1.1, thus increasing the probability of basal twin activation before the initiation of basal slip for the M plane. For loading rates utilized in the studies,[8,9] reduction in $\tau^{\text{Cr}}_{\text{basal tw}}(\dot{\varepsilon})$ due to increasing loading rates is insufficient to produce $\tau^{\text{Cr}}_{\text{basal tw}}(\dot{\varepsilon})/\tau^{\text{Cr}}_{\text{basal sl}}(\dot{\varepsilon})>0.9$ and, therefore, basal twinning cannot be activated before activation of basal slip for the A plane.

5. Determination of critical shear stress values for basal slip and basal twinning

Consideration of the values of $\tau^{\max}_{\text{basal tw}}$, $\tau^{\max}_{\text{basal sl}}$, and $\tau_{\text{basal tw}}/\tau_{\text{basal sl}}$ at P_{yield} for A and M planes discussed above indicates room-temperature values of $12.6\ \text{GPa}<\tau^{\text{Cr}}_{\text{basal tw}}<14.4$ GPa, $12.9\ \text{GPa}<\tau^{\text{Cr}}_{\text{basal sl}}<13.9$ GPa, and $0.9<\tau^{\text{Cr}}_{\text{basal tw}}/\tau^{\text{Cr}}_{\text{basal sl}}<1.1$. Less than 20% difference in $\tau^{\text{Cr}}_{\text{basal tw}}$ and $\tau^{\text{Cr}}_{\text{basal sl}}$ values predicted by the present analysis is consistent with the results of the study by Castaing *et al.*[33] indicating that critical shear stresses (CSSs) for basal slip and basal twinning are similar for $600\ ^\circ\text{C}<T<1200\ ^\circ\text{C}$. The present experiment-derived room-temperature $\tau^{\text{Cr}}_{\text{basal sl}}$ value is within the range of 4.8–23 GPa expected from the results of theoretical modeling and extrapolation of high-temperature experimental results reviewed by Tymiak and Gerberich[16] but higher than the recent results of nonlinear continuum modeling indicating the range of 2.7–5 GPa.[34] The present experiment-derived room-temperature $\tau^{\text{Cr}}_{\text{basal tw}}$ value is higher than 4 GPa estimated as a lower bound value by nonlinear continuum modeling[34] and exceeds range of 5.5–7.3 GPa predicted by the double-cross-slip model of basal twinning.[35] It is possible that $\tau^{\text{Cr}}_{\text{basal tw}}$ value obtained in the present study reflects the effect of very high levels of hydrostatic pressure generated under nanoindentation loading as discussed by Tymiak and Gerberich.[16] The results of molecular-dynamics (MD) study by Xu *et al.*[36] suggest that hydrostatic compression increases CSS for twinning. Modeling of indenter tip as a sphere might also be a source of inaccuracy of the present RSS results. Given indenter tip shape discussed in Sec. II A, parabolic rather than spherical surface might approximate actual indenter geometry more closely.

6. Activation of basal twins at loads significantly exceeding P_{yield}

With the presence of plastic deformation introducing considerable changes in the $\tau_{\text{basal tw}}$ and $\tau_{\text{basal sl}}$ distributions, conditions for activation of the post-yield-point sets of basal twins at the loads significantly exceeding the yield-point load can only be estimated with a significant degree of uncertainty. Assuming that the distributions $\tau_{\text{basal tw}}$ and $\tau_{\text{basal tw}}/\tau_{\text{basal sl}}$ after the yield point follow similar trends as prior to the onset of plasticity, it is reasonable to conclude that secondary sets of basal twins can be activated at the positions $\mathbf{a}_2$ in Fig. 3(a), $\mathbf{a}_0$ in Fig. 3(c), and $\mathbf{m}_0$ in Fig. 3(d) exhibiting localization of $\tau_{\text{basal tw}}$ and a favorable ratio $\tau_{\text{basal tw}}/\tau_{\text{basal sl}}>1.1$. Activation of secondary sets of basal twins would be consistent with the type 2a and type 2b AE signals observed for M and M planes at the loads 200–400 % of the yield-point load as shown in Fig. 1.

7. Remaining questions about plasticity initiation mechanisms

The present FEA evaluation points competitive processes of basal slip and basal twinning as the dominant yield-point

mechanism for *A* and *M* planes, respectively. However, several questions concerning loading-rate-dependent plasticity initiation mechanisms for *A* and *M* planes yet remain to be answered. The required clarifications include establishing the nature of a physical process giving rise to type 1c signals detected immediately after the activation of basal twinning for the *M* plane [Fig. 1(b), Table I]. It is possible that type 1c pattern corresponds to the initiation of slip accommodating boundaries of a newly activated twin. Such twinning-slip combination is observed during twinning in constrained crystals as discussed by Christian and Mahajan.[37] Accommodation of a twin boundary via formation of dislocation kinks is also possible.[37] While Basu *et al.*[15] proposed that the yield-point transition is governed exclusively by basal kinking, it appears more likely that basal kinking is one of the several processes involved in the yield point and that the incidence of basal kinking requires prior activation of twinning. Given its dependence on the twin geometry and stress state in the twin vicinity, peculiarities of slip activation in the vicinity of twin boundary are likely different from slip activation in a twin-free crystal. Therefore, differences of type 1c pattern from type 1a and type 1b pattern signals would be expected. However, in time domain, type 1c pattern signals seem indistinguishable from type 1a and type 1b pattern signals determined above to be signatures of basal slip as seen from Fig. 1. Similarly, time-domain representation offers no distinction between the type 2c pattern signals detected at the yield point as compared to type 2a and type 2b pattern signals detected at the loads significantly exceeding P_{yield}. The type 2a and 2b pattern signals were tentatively ascribed to activation of the post-yield-point sets of basal twins. Representation of type 1a, type 1b, type 1c, type 2a, type 2b, and type 2c pattern signals in JTFD discussed in Sec. III B serves as a step toward answering the questions expressed above.

B. AE signal analysis in joint time and frequency domain

The analysis was limited to discerning differences in JTFD representations of six signal categories specified in Table I. In order to minimize possible effects of overlap between type 1c and type 2c pattern signals, only type 1c and type 2c pattern signals detected as separate waveforms were analyzed. Type 1c and type 2c pattern signals detected as a single waveform such as shown in Fig. 1(b) were excluded from the evaluation because attenuation time of a type 2c pattern signal under such conditions was not exceeded at the start of a type 1c pattern signal.[38] Here, attenuation time was defined at the convergence of the integrated AE signal energy to a straight line corresponding to background noise level as detailed by Tymiak *et al.*[8]

Correlation of the JTFD characteristics of AE signals to the specific characteristics of the underlying physical processes (such as source type, source size, source time dependence, and source position with respect to the AE sensor surface) is beyond the scope of the present study. Such correlation would require calibration and deconvolution of the AE-sensing system response.[39]

The present authors assume that for the signals detected at the same AE-monitoring settings, the characteristic response of the AE system is the same and, consequently, differences in the observed AE signals result entirely from differences in the characteristics of the sources of corresponding physical events. Validity of such an assumption is supported by the specifics of the highly localized AE monitoring yielding signals essentially independent of the sizes and shapes of the evaluated samples.[8] Possible effects of indentation contact area on the detected AE signals is minimized by limiting comparative analysis to signals detected at approximately the same indentation loads.

AE signals representative of six subcategories of type 1 and type 2 pattern signals defined in Table I were selected and compared according to the above considerations. Overall, the results of JTFD analysis confirm the distinction between type 1 and type 2 pattern signal previously noted from time-domain evaluations.[8,9] JTFD representations (plotted at the same intensity scale) shown in Fig. 4 indicate that energy maps of type 1 and type 2 pattern signals differ most significantly in a frequency band centered at approximately 550 kHz. Time dependencies of 550 kHz frequency extracted from JTFD representations (as indicated by white dashed lines in Fig. 4) are plotted in Fig. 5. The frequency content profiles presented in Fig. 5 are normalized with respect to the maximum values for each signal indicated by arrows in JTFD maps shown in Fig. 4). Since the present JTFD representations are obtained without deconvolution of the response of AE-monitoring system, the prominence of the 550 kHz frequency band in the JTFD representations does not necessarily imply that this frequency band is dominant in the operation of the underlying physical sources.

As seen from Fig. 5(b), normalized 550 kHz frequency profiles of type 2a and type 2b pattern signals appear to follow the same trend as type 2c pattern signals determined to originate from activation of basal twinning. Starting from the beginning of a type 2 pattern signal, 550 kHz frequency content increases and reaches its maximum value after approximately 30 μs. Minor increase observed at estimated 45 μs after reaching the maximum evident from Fig. 5(b) suggests a two-stage underlying physical event mechanism. Similarity of the JTFD characteristics of the three subcategories of type 2 pattern signals discussed above is supportive of the assumption that those signals correspond to the same type of a physical process. However, a definite conclusion would need to be based on a more thorough analysis.

For the type 1 pattern signals, normalized 550 kHz frequency profiles reach maximum almost immediately and then decrease starting at 15 μs from the signal beginning. Overall, contribution of the 550 kHz frequency for the type 1 pattern signals is significantly smaller than for the type 2 pattern signals. Maximum of the normalized 550 kHz frequency content is 0.35–0.45 as compared to 0.5–0.75 for the type 2 pattern signals. While following common trends different from the tendencies exhibited by type 2 pattern signals, type 1a, type 1b, and type 1c pattern signals appear to exhibit subtle distinctions from each other.

Undistinguishable from type 1a and type 1b pattern signals in time domain, type 1c pattern differs from those signals in JTFD representation. As seen from Figs. 4(a)–4(c), type 1c pattern exhibits substantially lower content of 550 kHz frequency. The difference is even more apparent from

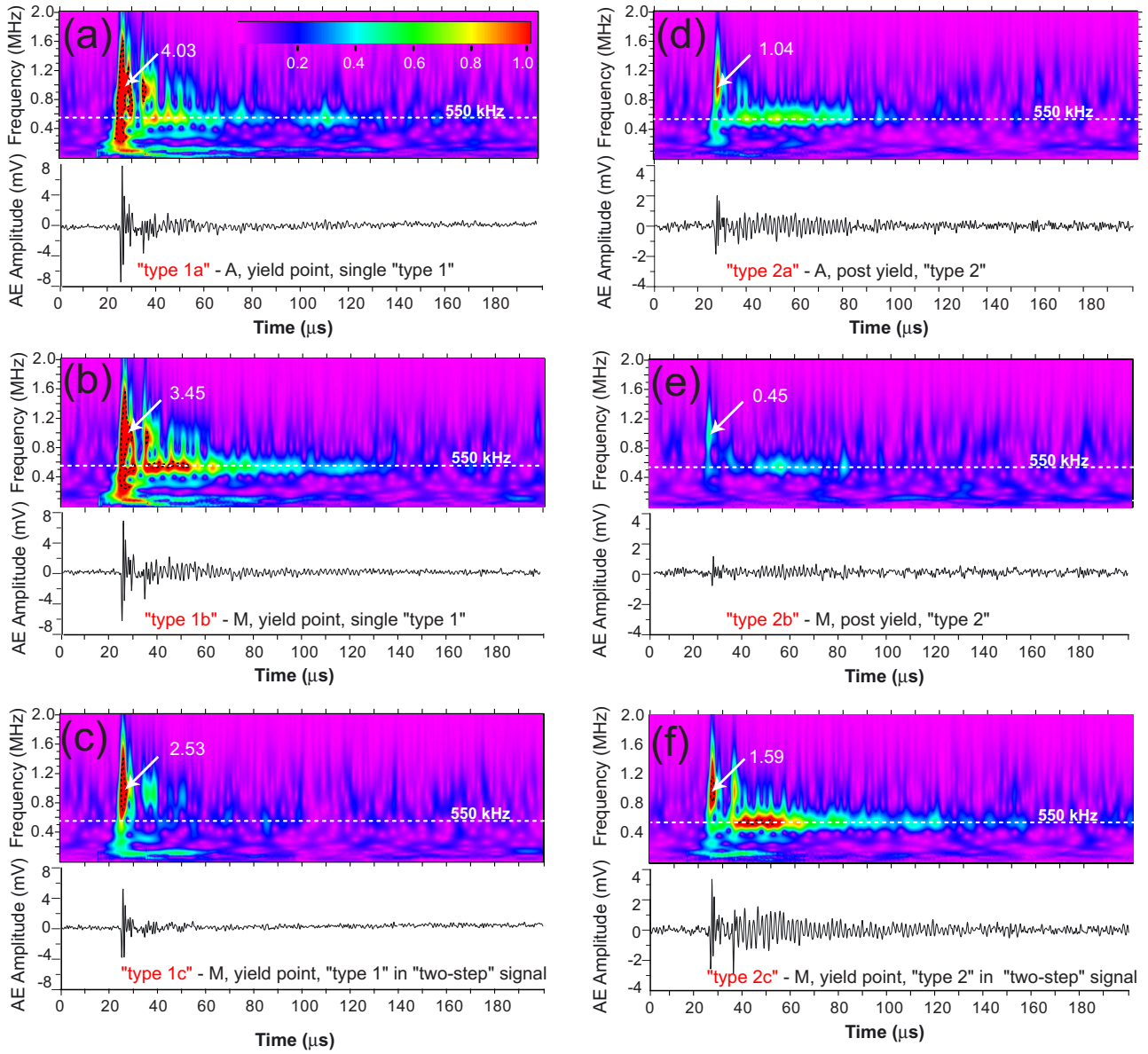

FIG. 4. (Color online) Comparison of AE waveforms representing six categories of AE signals defined in Table I. Signals previously ascribed to a single category type 1 pattern are shown in (a)–(c). Signals previously ascribed to a single category type 2 pattern are shown in (d)–(f). For each waveform, time-domain (bottom) and time-frequency-domain (top) representations are shown. All signals were detected in nanoindentation experiments with $P_{\text{yield}}=20.2$ mN and peak loads of 9 mN. Type 2 pattern signals shown in (e) and (f) were detected at indentation loads of 7 and 7.8 mN, respectively. Intensity scale is given in terms of wavelet transform coefficients (WTCs) obtained from wavelet decomposition of the examined AE signals (Ref. 32). WTCs represent arbitrary units scaling with the energy of the evaluated waveforms. In order to facilitate comparison between the presented AE signals, intensity scale was set the same by assigning an upper limit to 1 WTC through (a)–(f). For representations (a)–(c) and (f) with maximum intensity exceeding 1 WTC, black dotted lines outline regions where intensity is higher than 1 WTC (Ref. 38).

the frequency content profiles shown in Fig. 5(a). Noting that type 2 pattern signals follow a common trend independent of the maximum signal amplitude, a conclusion can be drawn that the observed distinction of type 1c pattern from type 1a and type 1b patterns cannot be justified solely by the lower amplitude of type 1c pattern signals. As discussed in Sec. III A 7, it is possible that type 1a and type 1b pattern signals correspond to basal slip initiation in a defect-free crystal, while type 1c pattern signal results from activation of slip accommodating boundaries of a newly formed twin. JTFD representations of type 1a and type 1b pattern signals detected at the yield point for *A* and *M* planes respectively do not seem to discern the differences between those signals as seen from Figs. 4(a) and 4(b). However, as evident from Fig. 5(a), content of 500 kHz frequency is slightly higher for the type 1b pattern signal.

The initial JTFD analysis discussed above does not provide definite answers regarding characteristics of the underlying physical sources. However, the JTFD analysis offers information not available from time-domain analysis.[8,9] This

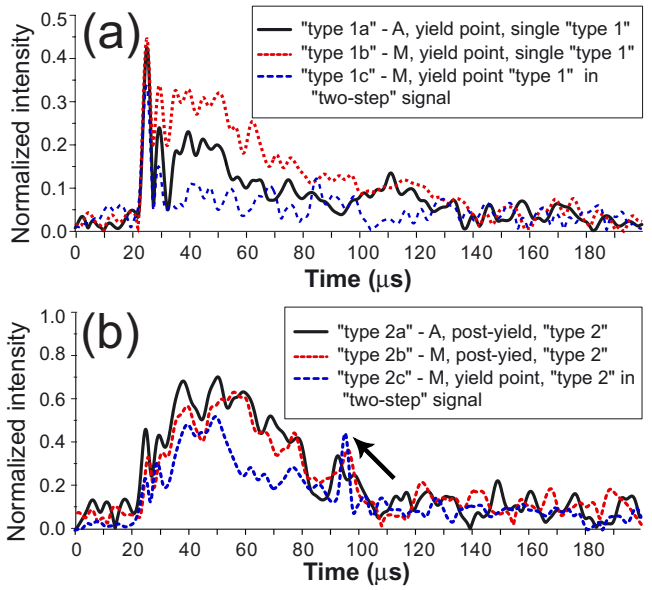

FIG. 5. (Color online) Change in the normalized contribution from 550 kHz frequency over signal time span (a) for type 1 pattern signals and (b) for type 2 pattern signals. The plotted frequency profiles correspond to sections denoted by white dashed lines in JTFD representations (Fig. 4). For each signal, frequency profile is normalized with respect to the maximum value for this signal indicated by white arrows in JTFD representations (Fig. 4).

includes the possibility of a two-step process giving rise to type 2 pattern signals as seen from Fig. 5(b) and the distinction between the three different subcategories of type 1 pattern signals evident from Fig. 5(a). The distinctions discerned in Fig. 5(a) may result from differences in the combination of underlying physical events and/or from differences in the distance or orientation of the source(s) of physical events with respect to the area of indentation contact effectively serving as AE-sensing area. The next level of JTFD analysis needs to provide more precise information about the physical processes giving rise to the detected AE signals. This requires deconvolution of the response of AE-sensing system[40] and modeling of AE activity originating from physical sources of different type, time dependence, and position with respect to the area of indentation contact.

C. Further verification and development of the proposed modeling

Finite element RSS analysis serves as a foundation for the present model justifying the effects of loading rate and surface orientation on the yield-point mechanism in sapphire[8,9,14,18,41] not explained by the previous models.[3,14,15] However, based on the analysis of RSS distributions at the yield point exclusively, it is not possible to prove that the yield-point mechanism is slip or twinning dominated, depending on surface orientation and/or loading rate. While the observed patterns of AE activity support the proposed model, *in situ* observations of contact-induced changes in crystal lattice during the yield-point would be required to unambiguously establish the yield-point mechanisms.

Transmission electron microscopy (TEM) evaluation of plastic zone generated in a test involving unloading immediately after the yield point might be considered as a possibility of direct verification of the proposed yield-point mechanisms. Such evaluations are not attainable yet due to the small scale of plastic deformation involved. Possibilities of reversible plasticity under nanoscale indentation contacts[42] and/or altering the original plasticity configuration during TEM sample preparation pose additional challenges. A detrimental downside of *in situ* TEM of nanoindentation[43,44] is that geometry of the evaluated system is not representative of indentation into a bulk material with the consequence of introducing plastic deformation modes different from those generated in bulk material.[43]

With the recent strides in atomistic modeling of contact-induced plasticity in ceramic crystals,[45–49] MD simulation of nanoscale contacts in Al_2O_3 reflecting all the complexity of the onset of plasticity is the anticipated advance. The study by Nishimura *et al.*[50] provides the initial much needed step in this direction. The next step would be an atomistic model fully reflecting the experimentally observed modes of contact-induced plastic deformation[51] in sapphire including slip, twinning, and phase transformations.[52]

IV. SUMMARY AND CONCLUSIONS

Prior experimental studies of acoustic emission-monitored nanoindentation experiments[8,9] suggest competitive processes of basal twinning as dominant yield-point mechanisms for *A* and *M* planes of sapphire.

The present study evaluates the possibility of basal slip-dominated vs basal twinning-dominated yield-point transition by performing FEA of RSS acting on basal slip and basal twinning systems. It is assumed that at a given strain rate $\dot{\varepsilon}$ activation of basal twinning before the initiation of basal slip requires sufficient localization of $\tau_{\text{basal tw}}$ (RSS for basal twinning), $\tau_{\text{basal tw}} \geq \tau^{\text{Cr}}_{\text{basal tw}}(\dot{\varepsilon})$, and $\tau_{\text{basal tw}}/\tau_{\text{basal sl}} > \tau^{\text{Cr}}_{\text{basal tw}}(\dot{\varepsilon})/\tau^{\text{Cr}}_{\text{basal sl}}(\dot{\varepsilon})$. Application of the above considerations justifies the experimentally observed patterns of surface traces of basal twins and indicates that conditions for activating basal twinning are more favorable for the *M* plane. Consequently, at sufficiently high loading rates, the yield-point mechanism for the *M* plane is dominated by basal twinning. In contrast, for the *A* plane, the yield-point transition is defined by activation of basal slip at least for the range of indentation loading rates utilized up to present.[9] Less than a 20% difference in $\tau^{\text{Cr}}_{\text{basal tw}}$ and $\tau^{\text{Cr}}_{\text{basal sl}}$ values as predicted by the present analysis is consistent with the results of the study by Castaing *et al.*[33]

Analysis of AE signals in JTFD allows discerning peculiarities of AE activity not apparent from time domain evaluations. Additional information provided by JTFD representation includes change in frequency content over lifespan of the evaluated signal.[7,26,32] JTFD representations emphasize the difference between the two types of AE signals, type 1 pattern and type 2 pattern previously ascribed[9] to basal slip and basal twinning, respectively. JTFD representations indicate that energy maps of type 1 and type 2 pattern signals differ most significantly in a frequency band centered at ap-

proximately 550 kHz. Consistent with the activation of the post-yield-point sets of basal twins at loads significantly exceeding the yield-point load, JTFD maps show no distinction between the type 2 pattern signals detected at the yield point and type 2 pattern signals detected at the loads 200–400 % exceeding the yield-point load. JTFD analysis of type 1 pattern signals indicate two different subtypes, one of which might be attributed to activation of basal slip in a twin-free region and another one which likely stems from slip activated to accommodate boundary of a newly activated twin.

It is stressed that *in situ* observations of contact-induced changes in the crystal lattice involved in the yield-point transition would be required to verify predictions of the proposed model. As transmission electron microscopy of the plastic zone immediately after the nanoindentation-induced yield-point transition in a bulk material is not currently attainable, atomistic modeling and advanced AE signal analysis are proposed. This would allow further verification of the proposed modeling and gain additional insights into the onset of contact-induced plasticity in sapphire.

Note added in proof. Recently published results by Nishimura *et al.* [Appl. Phys. Lett. **94**, 146102 (2009)] obtained by performing molecular dynamics and quantum mechanical calculations suggest that ideal shear strength of basal plane ranges from 16.3–18.9 GPa. The estimate of critical shear stress, 12.9–13.9 GPa, for basal slip obtained in the present study appears to be closer to the above atomistic calculations than to 2.7–5 GPa predicted by nonlinear continuum modeling.[34]

ACKNOWLEDGMENTS

The present research was supported by the Academy of Finland (through Research Projects NAKAMA and NANOTOMO) and by the Research Foundation of the Helsinki University of Technology. One of us (W.G.) would like to acknowledge support of the Air Force Office of Scientific Research through an AOARD program dedicated to understanding plasticity and fracture of hard materials. The calculations were performed at the Centre for Scientific Computing (CSC), Finland.

*tymiakni@yahoo.com
†On leave from Institute of Materials Science, University of Silesia, 40-007 Katowice, Poland.
‡rnowak@cc.hut.fi

[1] H. Gao, F. Yan, Y. Zhang, J. Li, Y. Zeng, and G. Wang, J. Phys. D **41**, 115106 (2008).
[2] P. Cain, Mater. Today **8**, 13 (2005).
[3] T. Page, W. Oliver, and C. McHargue, J. Mater. Res. **7**, 450 (1992).
[4] W. Gerberich, J. Nelson, E. Lilleodden, P. Anderson, and J. Wyrobek, Acta Mater. **44**, 3585 (1996).
[5] T. Michalske and J. Houston, Acta Mater. **46**, 391 (1998).
[6] A. Gouldstone, K. Van Vliet, and S. Suresh, Nature (London) **411**, 656 (2001).
[7] A. Daugela, H. Kutomi, and J. Wyrobek, Z. Metallkd. **92**, 1052 (2001).
[8] N. I. Tymiak, A. Daugela, O. L. Warren, and T. J. Wyrobek, J. Mater. Res. **18**, 784 (2003).
[9] N. I. Tymiak, A. Daugela, T. J. Wyrobek, and O. L. Warren, Acta Mater. **52**, 553 (2004).
[10] E. G-Berasategui, S. J. Bull, and T. F. Page, Thin Solid Films **447-448**, 26 (2004).
[11] J. M. Jungk, B. L. Boyce, T. E. Bucheit, T. A. Friedman, D. Yang, and W. W. Gerberich, Acta Mater. **54**, 4043 (2006).
[12] H. Bei, E. P. George, J. L. Hay, and G. M. Pharr, Phys. Rev. Lett. **95**, 045501 (2005).
[13] R. Nowak, T. Manninen, K. Heiskanen, T. Sekino, A. Hikasa, K. Niihara, and T. Takagi, Appl. Phys. Lett. **83**, 5214 (2003).
[14] R. Nowak, T. Sekino, S. Maruno, and K. Niihara, Appl. Phys. Lett. **68**, 1063 (1996).
[15] S. Basu, M. W. Barsoum, and S. R. Kalidindi, J. Appl. Phys. **99**, 063501 (2006).
[16] N. I. Tymiak and W. W. Gerberich, Philos. Mag. **87**, 5143 (2007).
[17] N. I. Tymiak and W. W. Gerberich, Philos. Mag. **87**, 5169 (2007).
[18] R. Nowak, T. Sekino, and K. Niihara, Acta Mater. **47**, 4329 (1999).
[19] P. Pirouz, B. F. Lawlor, T. Geipel, J. B. Bilde-Sørensen, A. H. Heuer, and K. P. D. Lagerlöf, Acta Mater. **44**, 2153 (1996).
[20] S. L. Van Doren, R. B. Pond, Sr., and R. E. Green, Jr., J. Appl. Phys. **47**, 4343 (1976).
[21] V. N. Bovenko, V. I. Polunin, and L. S. Soldatchenkova, Mater. Sci. **14**, 44 (1978).
[22] T. Richeton, P. Dobron, F. Chmelik, J. Weiss, and F. Louchet, Mater. Sci. Eng., A **424**, 190 (2006).
[23] J. B. Bilde-Sørensen, B. Lawlor, T. Geipel, P. Pirouz, A. Heuer, and K. Lagerlöf, Acta Mater. **44**, 2145 (1996).
[24] R. L. Bell and R. W. Cahn, Acta Metall. **1**, 752 (1953).
[25] S. Qian and D. Chen, IEEE Signal Process. Mag. **16**, 52 (1999).
[26] M. Iwanaga, Phys. Rev. B **72**, 012509 (2005).
[27] J. M. Winey and Y. M. Gupta, J. Appl. Phys. **90**, 3109 (2001).
[28] W. C. Oliver and G. M. Pharr, J. Mater. Res. **19**, 3 (2004).
[29] A. L. Yurkov, V. N. Skvortsov, I. A. Buyanovsky, and R. M. Matvievsky, J. Mater. Sci. Lett. **16**, 1370 (1997).
[30] D. Maugis, *Contact, Adhesion, and Rupture of Elastic Solids*, Springer Series in Solid-State Sciences Vol. 130 (Springer, Berlin, 1999).
[31] http://www.vallen.de
[32] H. Suzuki, T. Kinjo, Y. Hayashi, M. Takemoto, K. Ono, and Y. Hayashi, J. Acoust. Emiss. **14**, 69 (1996).
[33] J. Castaing, A. He, K. P. D. Lagerlöf, and A. H. Heuer, Philos. Mag. **84**, 1113 (2004).
[34] J. D. Clayton, Proc. R. Soc. London, Ser. A **465**, 307 (2009).
[35] K. P. D. Lagerlöf, J. Castaing, P. Pirouz, and A. H. Heuer, Philos. Mag. A **82**, 2841 (2002).
[36] D.-S. Xu, J.-P. Chang, J. Li, R. Yang, D. Li, and S. Yip, Mater. Sci. Eng., A **387-389**, 840 (2004).

[37] J. W. Christian and S. Mahajan, Prog. Mater. Sci. **39**, 1 (1995).
[38] See EPAPS Document No. E-PRBMDO-79-092913 for further details of AE signal analysis. Plot of integrated AE energy indicating overlap between type 2c and type 1c patterns detected in a single waveform is shown in Supplemental Fig. 1. JTFD representations with the upper limits set to individual maximum WTC values are shown in Supplementary Fig. 2. For more information on EPAPS, see http://www.aip.org/pubservs/epaps.html
[39] M. Enoki and T. Kishi, Int. J. Fract. **38**, 295 (1988).
[40] T. Kishi and M. Enoki, *Fracture Mechanics* (Elsevier Applied Sciences, London, 1991), pp. 217–234.
[41] R. Nowak and M. Sakai, Acta Metall. Mater. **42**, 2879 (1994).
[42] W. W. Gerberich, W. M. Mook, M. J. Cordill, C. B. Carter, C. R. Perrey, J. V. Heberlein, and S. L. Girshick, Int. J. Plast. **21**, 2391 (2005).
[43] A. M. Minor, E. T. Lilleodden, M. Jin, E. A. Stach, D. C. Chrzan, and J. W. Morris, Philos. Mag. **85**, 323 (2005).
[44] O. L. Warren, Z. Shan, S. A. S. Asif, E. A. Stach, J. W. Morris, Jr., and A. M. Minor, Mater. Today **10**, 59 (2007).
[45] I. Szlufarska, R. K. Kalia, A. Nakano, and P. Vashishta, Appl. Phys. Lett. **85**, 378 (2004).
[46] J. Li, K. J. Van Vliet, T. Zhu, S. Yip, and S. Suresh, Nature (London) **418**, 307 (2002).
[47] D. Chrobak, K. Nordlund, and R. Nowak, Phys. Rev. Lett. **98**, 045502 (2007).
[48] P. Valentini, W. W. Gerberich, and T. Dumitricã, Phys. Rev. Lett. **99**, 175701 (2007).
[49] R. Nowak, D. Chrobak, S. Nagao, D. Vodnick, M. Berg, A. Tukiainen, and M. Pessa, Nature Nanotech. **4**, 287 (2009).
[50] K. Nishimura, R. K. Kalia, A. Nakano, and P. Vashishta, Appl. Phys. Lett. **92**, 161904 (2008).
[51] N. Tymiak, D. Chrobak, S. Nagao, K. Nordlund, J. Räisänen, W. Gerberich, and R. Nowak, Appl. Phys. Lett. **94**, 146101 (2009).
[52] T. Wermelinger, C. Borgia, C. Solenthaler, and R. Spolenak, Acta Mater. **55**, 4657 (2007).